37

Preparation and Characterization of Dielectric Thin Films by RF Magnetron-Sputtering with $(Ba_{0.3}Sr_{0.7})(Zn_{1/3}Nb_{2/3})O_3$ Ceramic Target

Feng Shi
College of Physics & Electronics, Shandong Normal University, P.R. China

1. Introduction

Barium-strontium-zinc niobate (BSZN) [$(Ba_xSr_{1-x})(Zn_{1/3}Nb_{2/3})O_3$, where x is the mole fraction and $0 \le x \le 1$] is one of the $A\left(B'_{1/3}B''_{2/3}\right)O_3$ type microwave dielectric ceramics which have many advantage properties at very high microwave frequency, such as extremely low dielectric loss and near zero temperature coefficient of resonance frequency with low cost (Xu et al., 2006; Yu et al., 2006; Ianculescu et al., 2007; Huang et al., 2006; Varma et al., 2006). Due to these properties, BSZN has several potential applications in the fields of satellite communication and radar and mobile communication systems. As promising materials used in microelectronic and microwave integration circuit, microwave dielectric ceramic thin films will attract great attention in the near future (Huang et al., 2006).

Radio frequency (RF) magnetron sputtering is a dominant technique to grow thin films because a large quantity of thin films can be prepared at relatively high purity and low cost. The growth of thin films using $(Ba_xSr_{1-x})(Zn_{1/3}Nb_{2/3})O_3$ microwave dielectric ceramic as target materials has not been reported all over the world except my group (Cui et al., 2010; Shi et al., 2010) and there is very little information for direct reference. In this article, the thin films were initially prepared by radio frequency magnetron sputtering system using sintered $(Ba_xSr_{1-x})(Zn_{1/3}Nb_{2/3})O_3$ microwave dielectric ceramic as target. Then the deposited samples were annealed in oxygen ambience at different powers of 150 W, 200 W, and 250 W, different pressures of 0.1 Pa, 0.25 Pa, 0.5 Pa, 0.7 Pa, and 1.0 Pa, different annealing temperatures of 850 ℃, 1000 ℃, and 1150 ℃ and different annealing times of 15 min, 30 min, 45 min, and 60 min. The microstructure, components and surface morphology properties are investigated in detail, and the effect of experimental conditions on the growth of the thin films is studied in particular.

2. Experimental procedure

Ceramic thin films were deposited on SiO_2 (110) substrates by adopting sintered $(Ba_xSr_{1-x})(Zn_{1/3}Nb_{2/3})O_3$ microwave dielectric ceramics as sputtering target with a size of 62- × 3 mm in a JGP-450 radio frequency magnetron sputtering system. The SiO_2 (110) substrate was ultrasonically cleaned in an acetone and followed by rinsing in de-ionized

water several times. The chamber pressure was maintained at 1.0×10^{-3} Pa, and the argon gas (99.999%) was then introduced into the chamber. The distance between the target and the substrates was 11 cm, the substrate was heated to 610 °C and the sputtering time is 3 hrs per time. A post-deposition annealing was needed so that the deposited films have a well-crystallized structure. When the conventional tube furnace was heated up to a certain temperature, the quartz boat with the samples was placed into the constant temperature region. Then the flowing O_2 (99.999%) was introduced into the tube and the samples were annealed at O2 atmosphere with a flow rate of 500 ml/min. After being annealed, the samples were taken out for characterization.

A Rigaku D/max-rB X-ray diffraction (XRD) meter with Cu K_α-line, X-ray photoelectron spectroscope (XPS), a Hitachi S-450 scanning electron microscope (SEM), a Park Autoprobe CP atomic force microscope (AFM) and a Hitachi H-8010 transmission electron microscopy (TEM) were applied to characterize the microstructure, components and surface morphology properties of the thin films and to study their crystallinity. The morphology of cross-section of the thin film was examined by SEM (JEOL JSM-6390).

3. Results and discussion

3.1 Microstructure and components analysis

Figure 1 shows the X-ray diffraction patterns of the as-cast thin films at different powers (the sputtering pressure is 0.25 Pa).

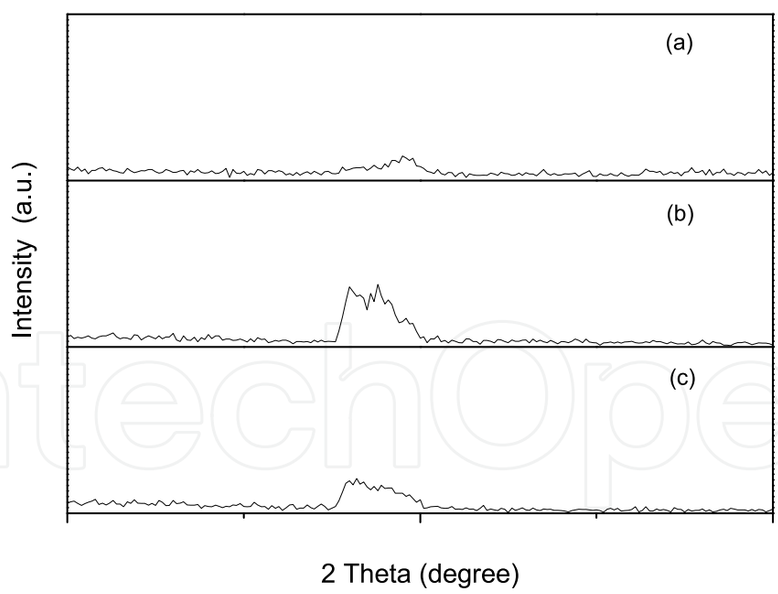

Fig. 1. X-ray diffraction patterns of the as-cast thin films at different powers.
(a) 150 W, (b) 200 W, (c) 250 W.

Figure 1 shows no diffraction peak exists, only three weak diffraction packets, which indicates that the thin films do not crystallize, but only exist in an amorphous state. The intensities and shapes are different obviously for these samples sputtered at different powers. The intensity is the strongest when sputtering power is 200 W.

Figure 2 shows the XRD spectra obtained from the thin films deposited at the pressure of 0.25 Pa, annealing at 1150 °C for 30 min and different powers of (a) 150 W, (b) 200 W, (c) 250 W.

In Figure 2 (a), there are a small number of diffraction peaks with low intensity in comparison to those of the other two samples. This phenomenon is due to the fact that the low kinetic energies of the sputtered-ejected ions are not sufficient for the arrangement and crystallization of particles on the substrates when sputtered at lower RF power (Wang et al., 2004). On the other hand, at 200 W (as shown in Figure 1 (b)), the amorphous thin films begin to crystallize, and more diffraction peaks appear in the sample with the strongest intensity. In Figure 2 (b), major peaks are identified to be $Ba_{0.5}Sr_{0.5}Nb_2O_6$ and $Ba_{0.27}Sr_{0.75}Nb_2O_{5.78}$ as compared with JCPDS files No. 39-0265 and No. 31-0166 (International Center for Diffraction Data, 2002), which is different from the target components.

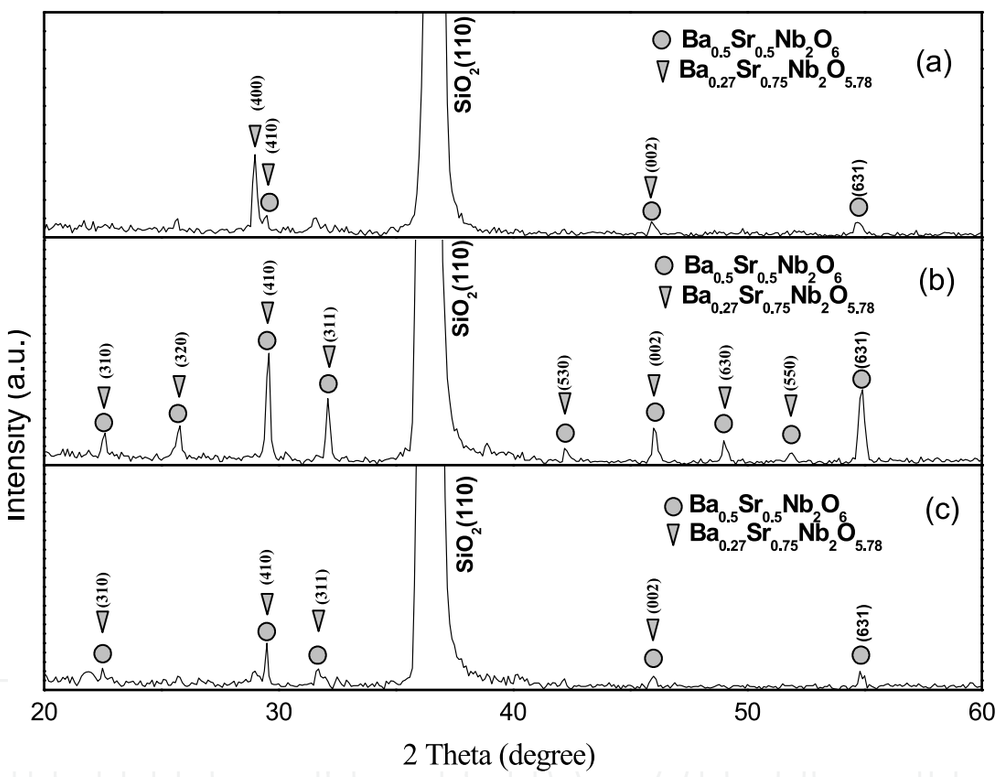

Fig. 2. X-ray diffraction patterns of the thin films deposited at 0.25 Pa and different powers: (a) 150 W, (b) 200 W, (c) 250 W.

These peaks are caused by the volatilization of ZnO during the process of sputtering and annealing; this is the same as that stated in reference (Huang et al., 2006). There is no preferential orientation for the thin films, i.e., they are randomly orientated. The diffraction peaks in every crystal plane of the films are almost complete, which indicates the grains have excellent crystal quality. When sputtered at 250 W (as shown in Figure 2 (c)), both the quantity and intensity of the thin film diffraction peaks are lower and weaker than that of the sample sputtered at 200 W. Both the crystal quality of the thin films and the intensity of the reflection peaks are at their best when the RF power is of 200 W, because the increase in kinetic energies of the sputter-ejected species accelerates the arrangement and crystallization

of particles on the substrate surface (Hsi et al., 2003). However, when the power is of 250 W, the kinetic energy of the sputter -ejected species is very high. As a result, the particles excited from the ceramic target were thrown away and not deposited on the substrate.

On the other hand, the greater the sputtering powers, the higher the kinetic energies, and the quicker the deposition rate. Deposition rate is lower at 150 W, and is higher at 250 W, i.e., appropriate deposition rate attributes to the film growth; therefore, 200 W is the optimum condition for the growth of the thin films.

In order to further investigate the growth of the thin films, the full-width at half-maximum (FWHM) of the (410) peaks of the $Ba_{0.5}Sr_{0.5}Nb_2O_6$ and $Ba_{0.27}Sr_{0.75}Nb_2O_{5.78}$ phases is analyzed. According to Scherrer`s formula (Klung et al., 1974), the grain size in (410) orientation can be estimated as follows:

$$L_{(410)} = \frac{k\lambda}{\beta_0 \cos\theta},$$

where k is a constant with a value of about 0.89 for Cu target, λ is the X-ray wavelength, β_0 is the FWHM of (410) peak, and θ is the diffraction angle. The estimated results are listed in Table 1.

Sample	(hkl)	2θ /^{0}	FWHM/rad	L/nm
B_1(150 w)	(410)	29.51	0.0061	24.1
B_2(200 w)	(410)	29.57	0.0043	36.3
B_3(250 w)	(410)	29.51	0.0050	30.6

Table 1. The grain size of $Ba_{0.5}Sr_{0.5}Nb_2O_6$ and $Ba_{0.27}Sr_{0.75}Nb_2O_{5.78}$ phases in the thin films estimated by Scherrer`s formula.

Therefore, with an increase in the sputtering power, the grains sizes of the thin films reach a maximum of 36.3 nm at 200 W and then decrease to 30.6 nm at 250 W.

Figure 3 shows X-ray diffraction patterns of the as-cast thin films and the samples annealing at different temperatures for 30 min (sputtered at 200 W and 0.25 Pa).

Figure 3 (a) indicates there is only a single crystal SiO_2 peak instead of diffraction peaks of other phases. It is well known that the formation of crystalline phase in thin films is affected by two important factors: one is the temperature in the sputtering process and the other is the annealing temperature. Therefore, during sputtering, the temperature of SiO_2 substrate, about 610 °C, is insufficient to initiate the formation of crystallization, thus the annealing treatment after sputtering is crucial. When the annealing temperature is 850 °C, as shown in Figure 3 (b), one weak peak appears, which is too weak to separate clearly and shows the thin film is in an amorphous state. But when the annealing temperature increases to 1000 °C, more and stronger peaks occur in Figure 3 (c). The main phases are also $Ba_{0.5}Sr_{0.5}Nb_2O_6$ and $Ba_{0.27}Sr_{0.75}Nb_2O_{5.78}$, but there is no peak of $(Ba_{0.3}Sr_{0.7})(Zn_{1/3}Nb_{2/3})O_3$. The difference between the components of the films and target attributes to the volatilization of ZnO during the process of sputtering and annealing, which is the same as that stated in Figure 2. The intensity of diffraction peak in Figure 3 (c) is stronger than that of the sample shown in

Figure 3 (b), because this thin film has transited from the amorphous state to the crystalline state at higher annealing temperature. When the annealing temperature increases to 1150 °C, as shown in Figure 3 (d), which is the same as Figure 2 (b), all peaks of crystal planes have appeared, which reveals that the thin film crystallizes completely, but there is no preferential growth. Moreover, the intensity of diffraction peak in Figure 3 (d) enhances greatly due to good crystallization at the highest annealing temperature. Figure 3 states there is steady growth for the strength and quantity of the thin film diffraction peaks with the increase in annealing temperature.

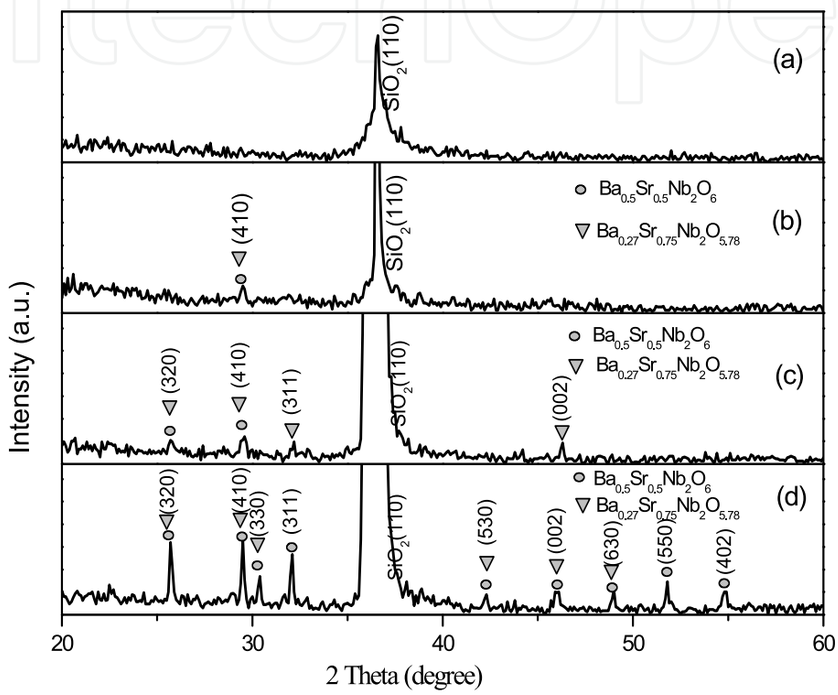

Fig. 3. X-ray diffraction patterns of the as-cast thin films and the thin films annealing at different temperatures for 30 min,(a) as-cast, (b) 850 ℃, (c) 1000 ℃, (d) 1150 ℃.

According to the (320), (410), and (330) peaks, through the formula (Wang et al., 2004) $d_{hkl} = \left[(h/a)^2 + (k/a)^2 + (l/c)^2 \right]^{-\frac{1}{2}}$, where d_{hkl} is interplanar crystal spacing, and h, k and l are crystal indices, we can calculate the lattice constants of $Ba_{0.5}Sr_{0.5}Nb_2O_6$ and $Ba_{0.27}Sr_{0.75}Nb_2O_{5.78}$ phases: a=b=12.456 Å and c=3.952 Å of $Ba_{0.5}Sr_{0.5}Nb_2O_6$ phase and a=b=12.430 Å and c=3.913 Å of $Ba_{0.27}Sr_{0.75}Nb_2O_{5.78}$ phase. A higher annealing temperature accelerates the material migration and diminishes the crystallographic defects and dislocations, thus promots crystallization of the thin films, and therefore, the excellent crystal structures are obtained accordingly.

The intensity is related with the crystallinity, the thickness of the thin films and the consistency, whereas the full width at half maximum (FWHM) value only reveals the crystallinity of the thin films. Due to different volatilization at different annealing temperatures, the thickness and consistency of peaks are different, therefore, the intensities of diffraction peaks are also different. Generally speaking, the annealing treatment can

promote atomic mobility and enhance the ability of atoms so that they can find the most energetically favored points; therefore, with the increase in the annealing temperature, the crystallographic defects including dislocations and vacancies in the thin films decrease rapidly, i.e., the appropriate annealing temperature is the key factor for a better crystal structure. The Scherrer formula (Schroeder et al., 1968) tells us that the smaller of the FWHM value, the better of the C-axis-preferred orientation, and the larger of the grain size and the better of the crystalline quality of the thin films. That is, the thin film which has the smallest FWHM value possesses the best crystalline quality and the largest grain size. The relation between FWHM and the annealing temperature is listed in Table 2.

Sample	phase	(hkl)	2θ /^{0}	FWHM/^{0}
B_1(850 °C)	$Ba_{0.5}Sr_{0.5}Nb_2O_6$ $Ba_{0.27}Sr_{0.75}Nb_2O_{5.78}$	(410)	29.6085	0.291
B_2(1000 °C)	$Ba_{0.5}Sr_{0.5}Nb_2O_6$ $Ba_{0.27}Sr_{0.75}Nb_2O_{5.78}$	(410)	29.6085	0.215
B_3(1150 °C)	$Ba_{0.5}Sr_{0.5}Nb_2O_6$ $Ba_{0.27}Sr_{0.75}Nb_2O_{5.78}$	(410)	29.6085	0.125

Table 2. The relation between FWHM and annealing temperatures of the samples.

As shown in Table 2, the value of FWHM decreases with the increase in annealing temperature. The sample annealed at 1150 °C has the smallest value of 0.125, which shows the best crystalline quality (Zheng et al., 1993), because the energy supplied from the outside environment during the annealing process is sufficient to make the films crystallize completely at higher temperature.

Figure 4 shows X-ray diffraction patterns of the thin films annealing at 1150 °C for different times (sputtered at 200 W and 0.25 Pa).

In Figure 4 (a), there is only one diffraction peak with low intensity, and the phase is $Ba_{0.27}Sr_{0.75}Nb_2O_{5.78}$. This thin film just began to crystallize at 1150 °C for 15 min, because there was no enough time for the atoms migration on the substrate surface (Zannetti et al., 1969; Yang et al., 1998). Figure 4 (b) is the same as shown in Figure 3 (d): there is no other peak, which indicates that the thin film has high purity. Figure 4 (c) shows the intensity and number of the diffraction peaks decrease greatly in comparison to that shown in Figure 4 (b) because of excess volatilization of ZnO and recrystallization of the grains at longer annealing time, and the trend is clear as seen in Figure 4 (d). A new phase has appeared, named $Ba_{5.75}Nb_{2.25}O_{11.375}$ in Figure 4 (c) and Figure 4 (d).

Figure 5 is the relation between the FWHM values and the grain sizes with the different annealing times.

Annealing for 15 min, the samples cannot crystallize because of deficiency of the heat energy for material migration, thus the FWHM value is large; whereas after annealing for longer time, such as 45 min and 60 min, more heat energy will lead to excess volatilization of ZnO and recrystallization of the grains, thus lessening the FWHM value. As for the sample annealing for 30 min, the FWHM value is at its minimum and the grain size is the largest with the best crystallinity, as compared with the other samples annealing for 15 min, 45 min, and 60 min, because of the sufficient heat energy supplied by the outside environment

improve crystallization of the thin films, but the heat energy is not excessive. That is, it is appropriate for the thin films being annealed for 30 min.

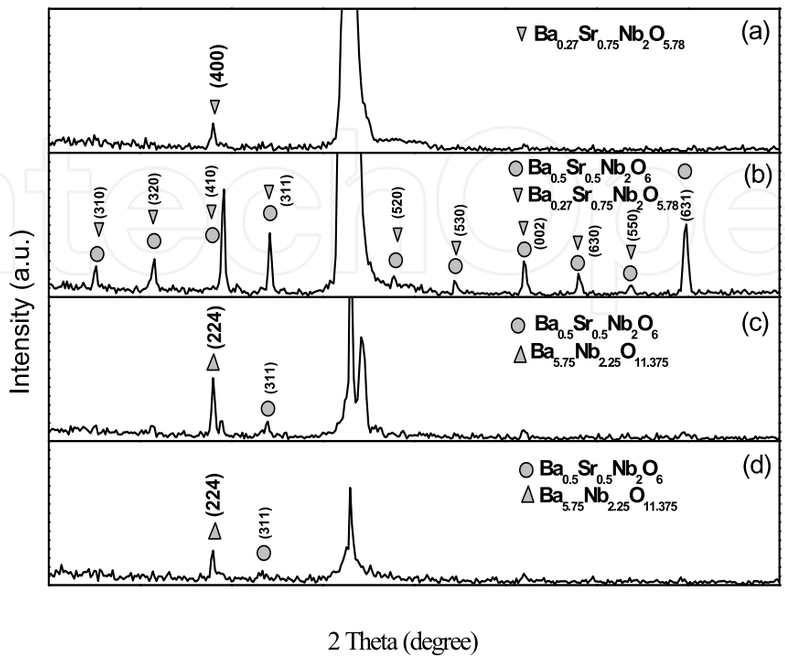

Fig. 4. X-ray diffraction patterns of the thin films annealing at 1150 °C for different times (sputtered at 200 w and 0.25 Pa).(a) 15 min, (b) 30 min, (c) 45 min, (d) 60 min.

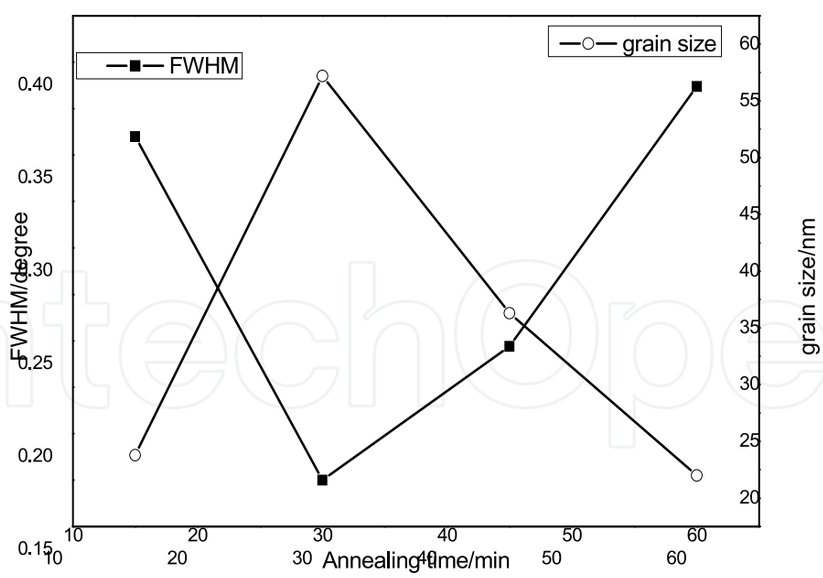

Fig. 5. The relation between the FWHM values and the grain size with the different annealing times.

Figure 6 shows X-ray diffraction patterns of the thin films at different pressures (sputtered at 200 W, annealing at 1150 °C for 30 min).

As seen from Figure 6, the trend is the same as that stated above in Figure 2 - Figure 4, i.e., the higher of the pressure, the lower of the intensity and the less of the number of the diffraction peaks. There is greater atomic density in vacuum chamber at higher gaseous pressure, i.e., the chances of atomic collision increase, and the energy loss of atoms is enhanced during material migration, thus lessening the quantity of the atoms reaching the substrate surface. The nucleation density decreases subsequently due to less particles; therefore, the growth of the thin films is weakened. The imbalance between Ba and Sr ions is closely related with saturated gaseous pressure, for instance, the stoichiometric ratio imbalance of Ba and Sr elements becomes inconspicuous at lower pressure as compared to the phases in Figure 6 (a), (b) and (c).

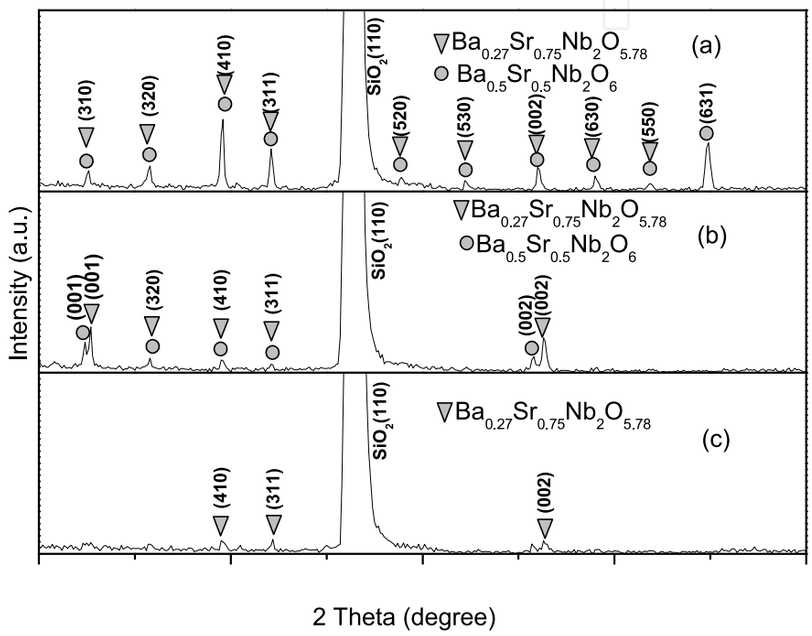

Fig. 6. X-ray diffraction patterns of the thin films at different pressures (sputtered at 200 W, annealed at 1150 °C for 30 min). (a) 0.25 Pa, (b) 0.50 Pa, (c) 0.70 Pa.

In Figure 6 (a), the grain growth is relatively complete, and therefore, more and stronger diffraction peaks appear. When the pressure increases to 0.5 Pa, the intensity and number of peaks decrease because of more collision among particles caused by higher pressure, thus material migration is inhibited and it's the same trend as the sample shown in Figure 6 (c).

According to the results of XRD, we pay much attention to the samples deposited at 150 W, 200 W, and 250 W (the sputtering pressure are of 0.25 Pa and annealed at 1150 ^{o}C for 30 min) and study their components; Figure 7 shows the XPS spectra of these samples. In Figure 7, the general scan of binding energy ranging from 0 to 1100 eV, the peaks of Sr3d, Nb3$p_{3/2}$, Ba3d, C1s, Nb3d, Zn3d and O1s are observed.

As seen in Figure 7, the main elements in the thin films are Ba, Sr, Nb, Zn, and O element. Since the samples selected for XPS analysis are exposed to the air, the elements of O and C arise from the thin film solution. O1s and C1s core level peaks are always detected, and O1s peak centers at 529.8 eV. Amanullah et al., (Amanullah et al., 1998) have reported that O1s

peak is usually observed in binding energy area of 529-535 eV; the peaks in 529-530 eV are ascribed to the lattice oxygen, the peaks for binding energy ranging from 530.0 eV to 530.9 eV correspond to chemisorbed oxygen, and therefore, the O1s peak corresponds to lattice oxygen. The peaks of C1s attribute to the standard sample during XPS testing. There is a weak peak corresponding to the Zn element in Figure 7, indicating that a part of Zn element exists in the thin film although the other part of ZnO is evaporated during the sputtering and annealing process, which is not consistent with the results shown in XRD because of the systematic error of the XRD.

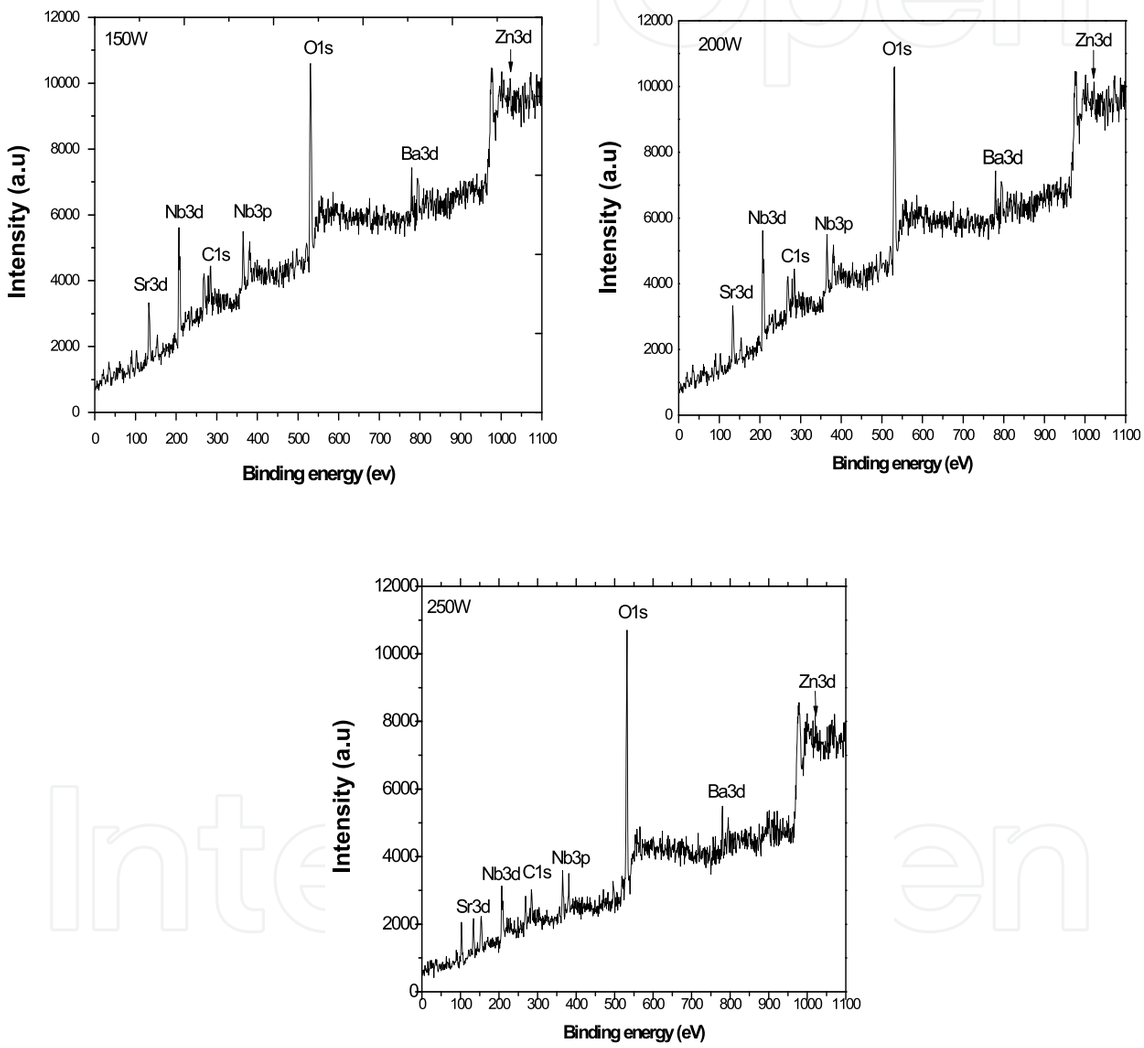

Fig. 7. XPS spectra obtained from the thin films deposited at 150 W, 200 W, and 250 W (0.25 Pa, 1150 °C, 30 min).

3.2 Morphology analysis

Figure 8 shows the typical SEM images of the samples sputtered at different powers and annealing at 1150 °C for 30 min (sputtering pressure: 0.25 Pa).

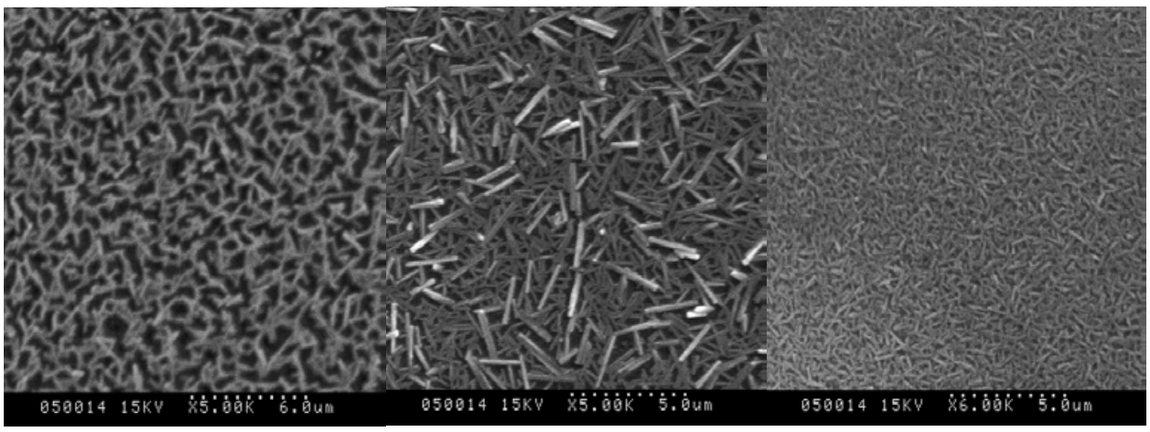

(a) (b) (c)

Fig. 8. Typical SEM images of the thin films sputtered at different powers. (a) 150 W, (b) 200 W, (c) 250 W.

When deposited at 150 W, the grains of the thin films have been formed with uniform and loose surface, and there are many holds on the thin film surface. During the coalescence stage of the sputtering process, fine particles do not have enough kinetic energy to grow into larger grains. After the annealing process, the thin films have changed from amorphous phase to crystal phase partially. Therefore, the intensities of diffraction peaks in XRD spectra are at their lowest, probably due to small deposition rate at 150 W. In Figure 8 (b), it is evident that the grains have well-defined boundaries around them and homogenously distribute on the substrates surface with uniform grain size. The grains are rod-like structures which form during the annealing process because the greater grains can combine with the smaller ones around them to generate rod-like grains. With higher energy gas plasma caused by higher RF power, more fine particles were sputtered from the target and these high-energy particles can migrate and combine together with each other on the substrate surface and form high quality crystalline films, which complies with the result of the XRD analysis (as shown in Figure 2 (b)). The sample in Figure 8 (c) is uniform and dense with strip shape grains, because adequate energy supplied during material migration promotes the formation of the thin films and crystallization of grains. Therefore, the thin films sputtered at higher powers possess perfect surface morphology.

Figure 9 shows the typical SEM images of the as-cast sample and the samples sputtered at 200 W, 0.25 Pa after annealing at different temperatures for 30 min.

As compared with the sample annealing at 1150 ^{o}C in Figure 8 (b), the as-cast sample (Figure 9 (a)) has a clean surface, but no grain; whereas when annealing at 850 ^{o}C, less grains appear; when the annealing temperature is 1000 ^{o}C, the amount of grains increases with fine particles covered on the surface. That is, crystallization is not complete at lower annealing temperature.

Figure 10 shows the SEM images of the samples sputtered at 200 W and 250 W, after annealing at 1150 ^{o}C for 45 min (sputtering pressure: 0.25 Pa).

In comparison to Figure 8 (b), there are more holes in Figure 10 (a) and the thin films are composed of block structures; this situation is similar to that shown in Figure 10 (b) and

Figure 8 (c). As seen in Figure 10 (b), the film is cracked and many gaps and holes exist among each fragmental structure, which attributes to recrystallization of grains due to longer material migration time.

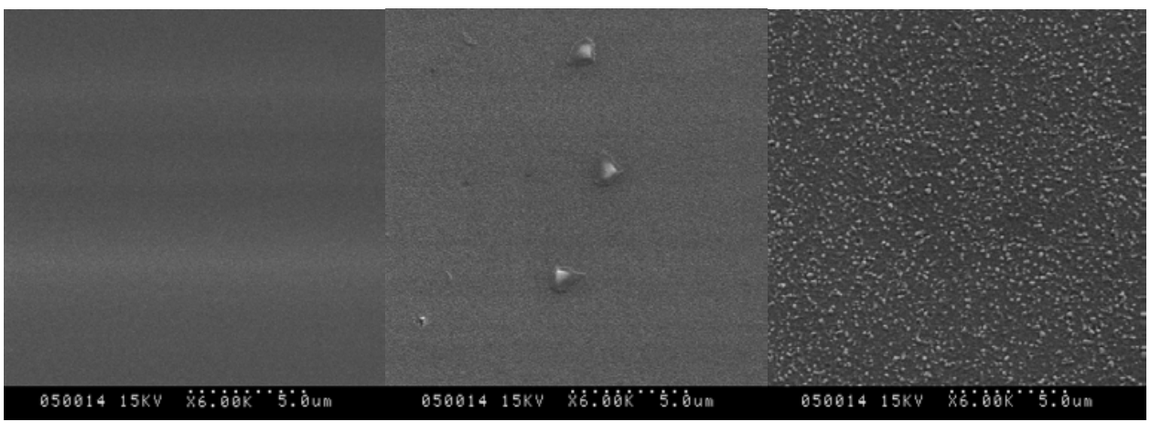

(a) (b) (c)

Fig. 9. Typical SEM images of the as-cast thin film and the thin films sputtered at 200 W, 0.25 Pa after annealing at different temperatures. (a) as-cast, (b) 850 °C, (c) 1000 °C.

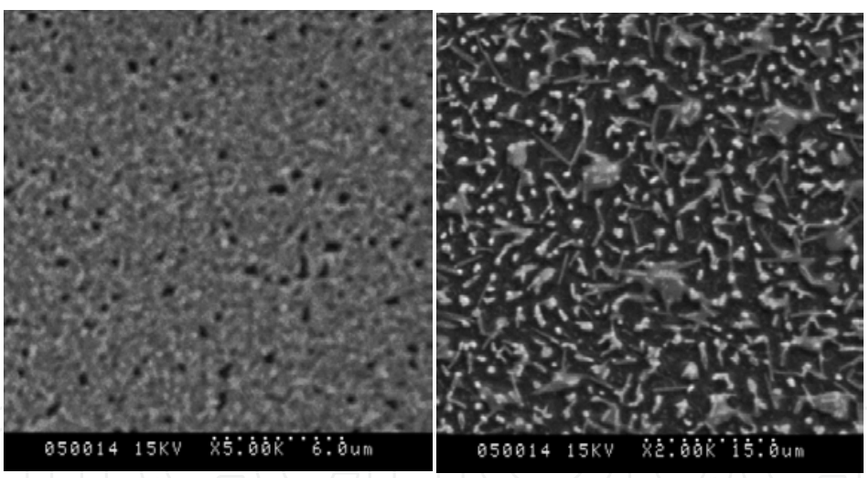

(a) (b)

Fig. 10. SEM images of the thin films sputtered at 200 W and 250 W, respectively, after annealing at 1150 °C for 45 min. (a)200 W, (b)250 W.

Figure 11 shows the SEM images of the samples sputtered at 200 W and different pressures of 0.10 Pa, 0.50 Pa, and 0.70 Pa, after annealing at 1150 °C for 30 min.

As seen from Figure 11, surface morphology differs with the sputtering gaseous pressures. Morphology shown in Figure 11 (a) is similar to that shown in Figure 8 (b), that is, the sample in Figure 11 (a) has perfect crystalline and surface morphology, which indicates that an appropriate low pressure can contribute to the film growth. With the increase of sputtering pressures, more holes and gaps form on the surface accompanied by the decrease

in grain size, which are shown in Figs.11 (b) and (c). During sputtering, the variation of sputtering gaseous pressure leads to the change of transmission capacity of Ba, Sr, Zn and Nb elements. The higher the sputtering gaseous pressure, the smaller the mean free path. When sputtered at lower pressures, the mean free path and transmission capacity of Ba, Sr, Zn and Nb elements increase, and particles sputtered to the substrate surface multiply rapidly (Wang et al., 2002; Liu et al., 2005). Therefore, the content of elements deposited on the surface increases at the lower pressure, and there are sufficient materials on the substrate surface which can promote the film growth and crystallization of grains. This conclusion can also be proved by Figure 12 as compared with Figure 8(c).

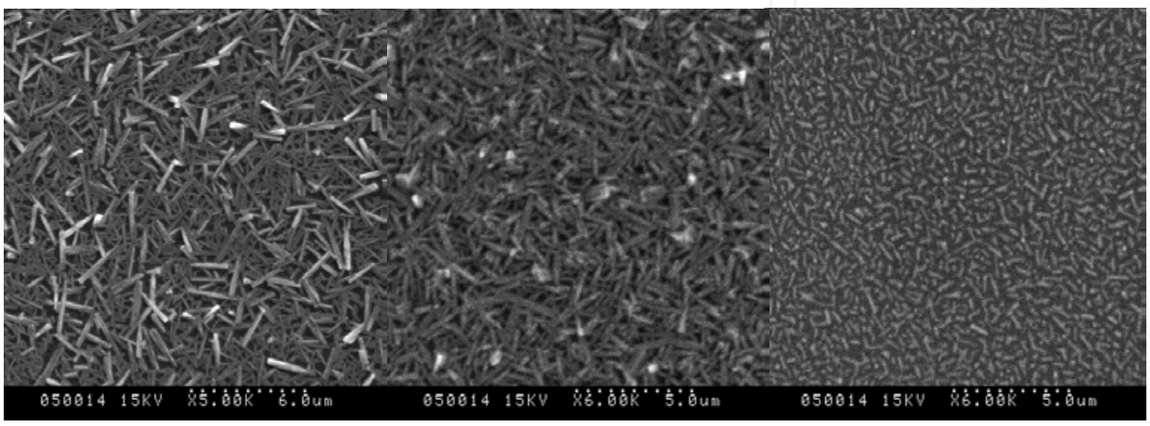

(a) (b) (c)

Fig. 11. SEM images of the thin films sputtered at 200 W and different pressures after annealing at 1150 °C for 30 min. (a) 0.10 Pa, (b) 0.50 Pa, (c) 0.70 Pa.

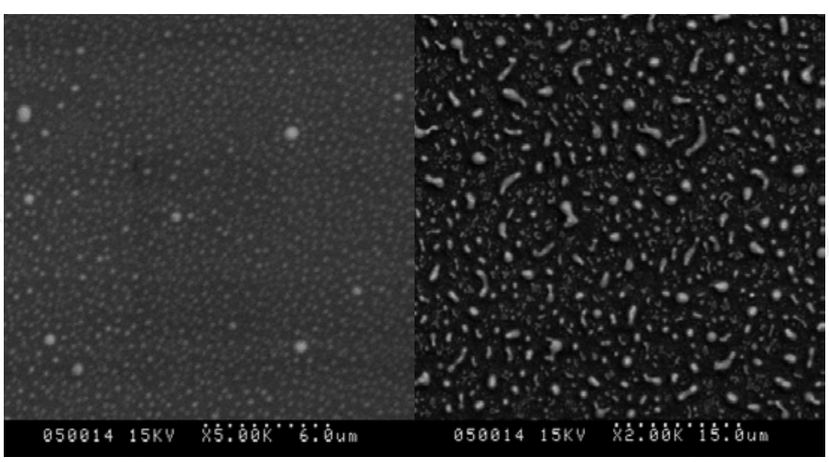

(a) (b)

Fig. 12. SEM images of the thin films sputtered at 250 W and different pressures annealing at 150 °C for 30 min, (a) 0.50 Pa, (b) 0.70 Pa.

Figure 13 shows the SEM micrograph of the cross section of the thin films prepared at 200 W, 0.25 Pa, with annealing 3 times (3 hrs per schedule) at 1150 °C for 30 min.

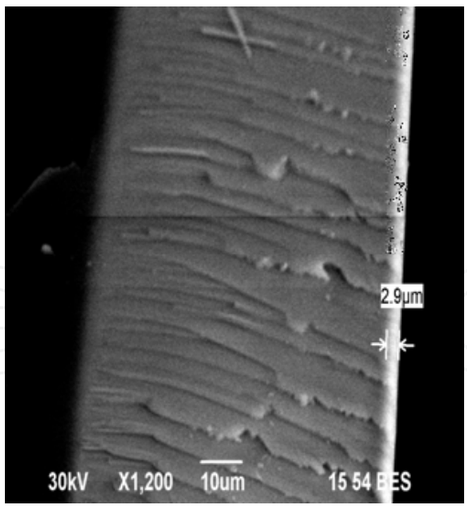

Fig. 13. The SEM micrograph of cross-section of the thin films deposited at 200 W for 3 times (3 hrs per schedule).

It can be seen that the thin film is dense and crack-free, with the thickness of 2.8 μm. That is, the thickness is about 0.9 um after sputtering for 3 hrs.

Figure 14 shows the AFM images of the as-cast thin film and the thin films deposited at 200 W, 0.25 Pa and annealing at different temperatures for 30 min (longitudinal cross-section).

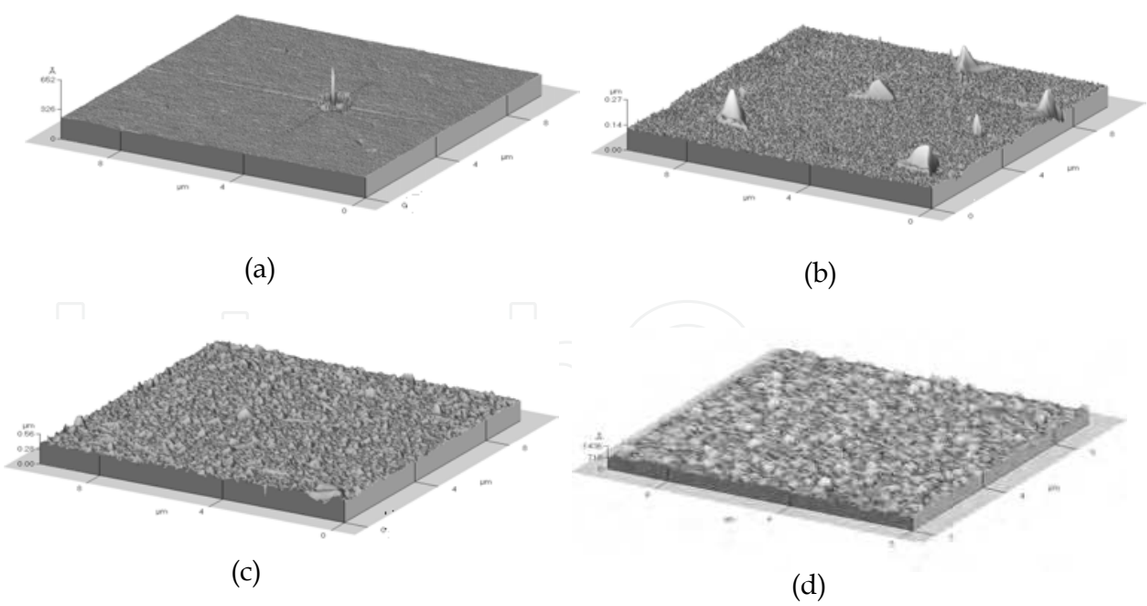

Fig. 14. AFM images of the as-cas thin film and the thin films deposited at 200 W and annealed at different temperatures for 30 min (longitudinal cross-section), (a)as-cast, (b) 850 °C, (c) 1000 °C, (d) 1150 °C

As shown in Figure 14, the grains on the surface of the samples become greater gradually with the increase of annealing temperature, which indicates that surface morphology and

crystallization of the grains depend on annealing temperature significantly – the higher the annealing temperature, the better the morphology and crystalline quality. Besides, the thin film surface becomes rougher with the increase in annealing temperature. Figure 14 also tells us the fact that the growth mechanism complies with the nucleus growth mode (Tang et al., 2003). At the beginning of the thin film growth, some atoms or molecules are deposited on the substrate surface and form the so-called nucleation phases. These atoms or molecules form some homogenous and fine atomic groups which can move and are called "islands". These islands can accept new atoms continuously and merge with other islands, and nascent islands could appear at the empty area at the same time, therefore, the amount of islands saturates quickly. The progress of formation and consolidation of islands was ongoing till these isolated islands combine into flakes, with less holes and gaps, which are filled with new atoms. Therefore, the continuous films form. The consolidation of islands ends when the thickness of the thin films is about several tens of nanometers (Tang et al., 2003).

Figure 15 shows the AFM images (horizontal cross-section) of the thin films deposited at different powers (0.25 Pa of sputtering pressure and annealing at 1150 °C for 30 min).

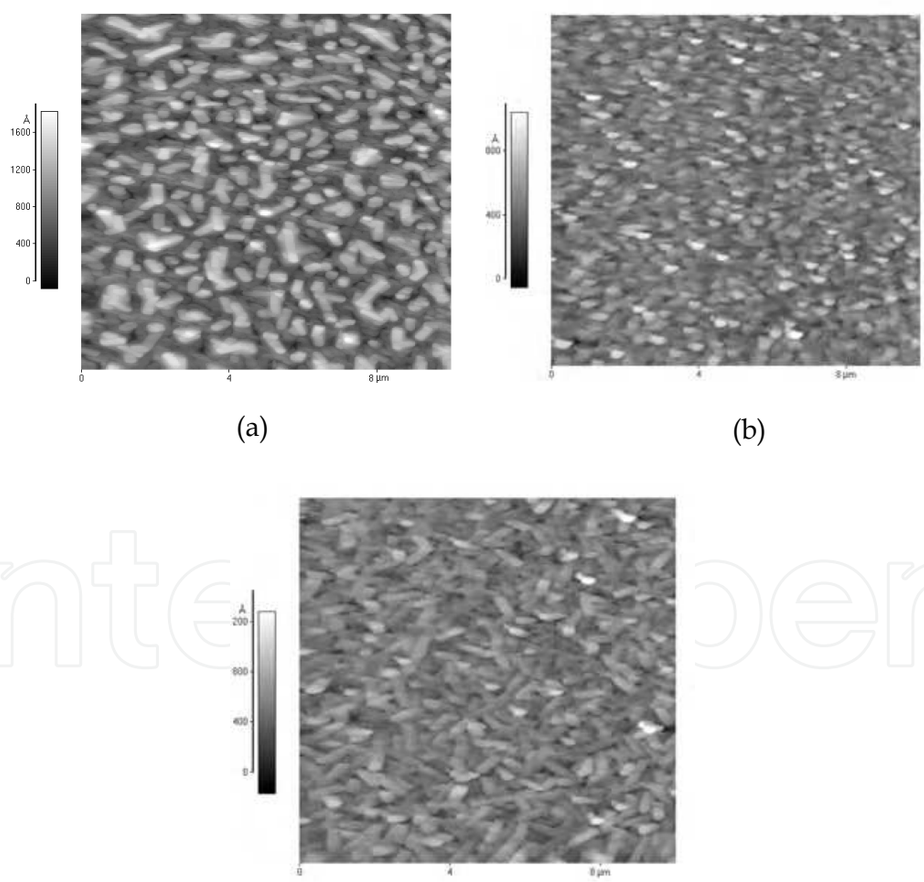

Fig. 15. AFM images (horizontal cross-section,10 µm×10 µm) of the thin films deposited at different RF powers: (a)150 W, (b) 200 W, (c) 250 W.

It is evident that different surface morphologies rely on sputtering powers significantly. Figure 15 (a) shows the surface morphology of the thin film at 150 W and the surface is smooth and compact with the smallest roughness. In Figure 15 (b), the film surface is obviously rough with high roughness value, and it can be seen that a few spikes grow along the c-axis that might have been caused by the agglomeration of the particles during crystallization of grains. Figure 15 shows that the films with high-quality crystalline form and the grain sizes of the thin films are at the greatest when the sputtering power is 200 W. The crystal quality is better for the sample deposited at 250 W than that of the sample deposited at 150 W, but worse than that of the sample deposited at 200 w. As seen from Figure 15 (c), the surface roughness is greater than that of the sample in Figure 15 (a), but less than that of the sample in Figure 15(b). As seen from Figure 15 (b) and (c), it can be inferred that the thin films consist of tightly packed particles with an average size of 92.8 nm and 58.5 nm, respectively. The grain size is considerably larger than that obtained by Scherrer`s formula from XRD. Obviously, each particle contains many single-crystal grains. In addition, the overall observation of the thin films indicate a superior microstructure for the thin films sputtered at 200 W, 0.25 Pa, after annealing at 1150 °C for 30 min.

Figure 16 shows the AFM images of the as-cast thin film and the films deposited at 200 W, 0.25 Pa and annealing at 1150 °C for different times (longitudinal cross-section).

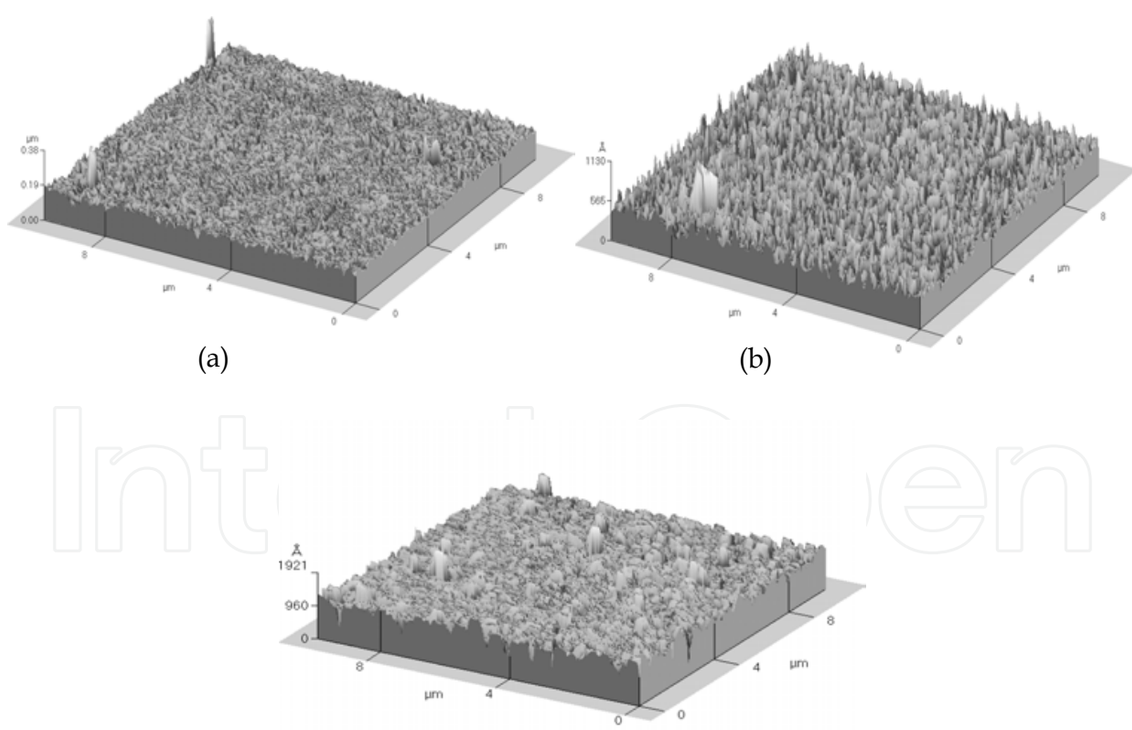

Fig. 16. AFM images of the as-cast thin film and the thin films deposited at 200 W and annealing at 1150 °C for different times (longitudinal cross-section).(a)15 min, (b) 45 min, (c) 60 min.

As compared with Figure 14 (d), Figure 16 reveals that the morphologies of the thin films are closely related with the annealing time and the roughness of the thin films changes greatly with the variation in the annealing times. Annealing after 15 min, surface irregularity appears but root-mean-square surface roughness (RMS, calculated from the AFM data using software) is lower than that of the sample in Figure 14 (d), because the time for material migration is not sufficient. While annealing after 45 min and 60 min, surface irregularities enhance and the roughness is larger than that of the sample in Figure 16 (a), due to availability of more time for material migration, but lower than that of the sample in Figure 14 (d), because of excess volatilization of ZnO and recrystallization of grains. That is, surface irregularities increase from 15 min to 30 min, and then decrease gradually from 30 min to 60 min, which is the same as that shown in Figure 17, the relation between RMS and annealing time.

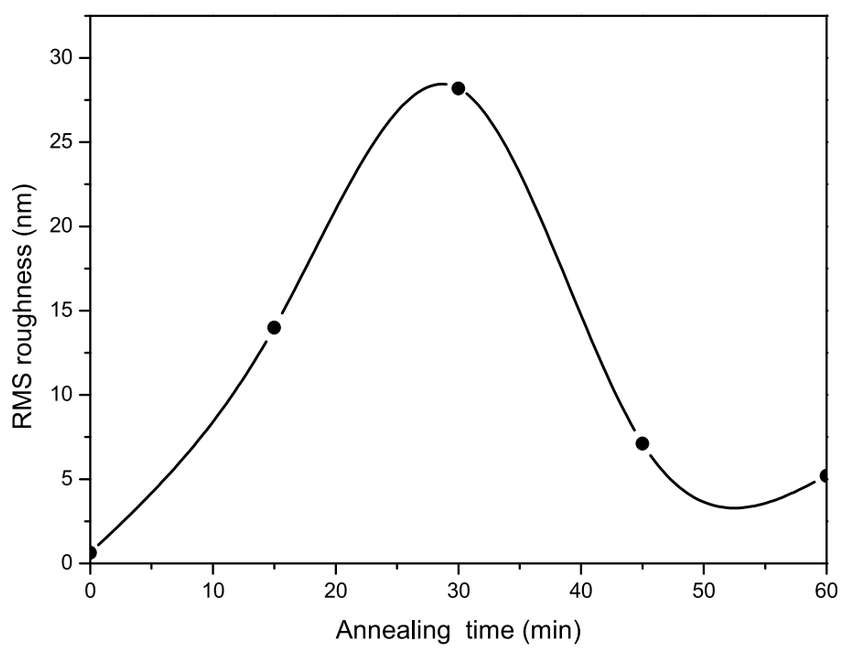

Fig. 17. Relation between RMS and annealing time.

Figure 17 shows that the roughness of the samples annealing after different times are 0.633 nm (as-cast), 14 nm (15 min), 28.2 nm (30 min), 7.12 nm (45 min), and 5.2 nm (60 min). Therefore, annealing times can affect RMS deeply, as the results show in Figure 5.

Transmission electron microscopy (TEM) is carried out for further investigating the crystal property of the sample deposited at 200 W, 0.25 Pa and annealing at 1150 ^{o}C for 30min, as shown in Figure 18. In Figure 18 (a), the grains are relatively straight, and the shape of most grains is rod-like structure, as indicated in Figure 8 (b). Figure 18 (b) shows the selected area electron diffraction (SAED) spectrum of the sample likes a ring, which indicates that the thin films are polycrystalline, and there are many flakes like dancing butterflies in Figure 18 (c), which indicates that the shape of the sample spurtered at 250 W is different from that shown in Figure 18 (b). The grain sizes in Figure 18 (b) are greater than that of the samples sputtered at 200 W.

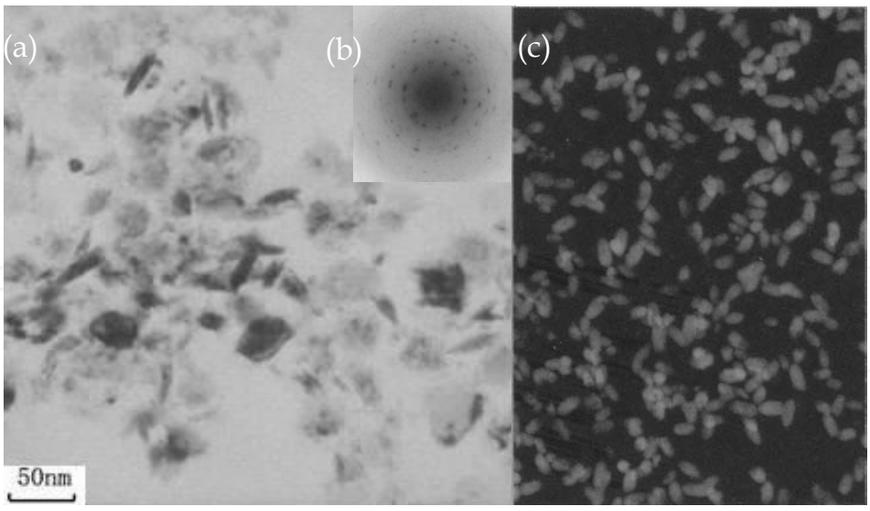

Fig. 18. (a) TEM image (bright field image) and (b) SAED spectrum of the thin film deposited at 200 W, 0.25 Pa and annealing at 1150 °C for 30 min. (c) TEM image (dark field image) of the thin film deposited at 250 W, 0.25 Pa and annealed at 1150 °C for 30 min.

4. Conclusion

The thin films were successfully fabricated on $SiO_2(110)$ substrates through radio frequency (RF) magnetron sputtering system using sintered $(Ba_{0.3}Sr_{0.7})(Zn_{1/3}Nb_{2/3})O_3$ microwave dielectric ceramics as sputtering target, and next annealing in O_2 ambient. The thin films cannot crystallize without annealing and the main phases after annealing at 1150 °C for 30 min are $Ba_{0.5}Sr_{0.5}Nb_2O_6$ and $Ba_{0.27}Sr_{0.75}Nb_2O_{5.78}$ with less $Ba_{5.75}Nb_{2.25}O_{11.375}$, and the difference between the ceramic target and the thin films arises from the Zn loss through volitilization during sputtering and annealing process. The experimental conditions of sputtering powers, annealing temperatures, annealing times and sputtering pressures have deep influence on the microstructures and morphologies of the thin films. The samples deposited at 200 W, 0.25 Pa, and annealed at 1150 °C for 30 min have the highest crystalline quality. This thin film is polycrystalline with a dense and rod-like structure. The growth mechanism complies with the nucleus growth mode.

5. Using Zn - enriched $(Ba_{0.3}Sr_{0.7})(Zn_{1/3}Nb_{2/3})O_3$ as Target

5.1 Introduction

To obtain a dense thin film with fewer oxygen vacancies and less Zn loss, in this article, we adjusted the target component to fabricate ceramic thin films using magnetron sputtering deposition, which differs from those targets reported previously (Cui et al., 2010; Shi et al., 2010), i.e., 1 mol excess ZnO was incorporate in this stoichiometric $(Ba_{0.3}Sr_{0.7})(Zn_{1/3}Nb_{2/3})O_3$ target so as to compensate the ZnO volatilization during the sputtering and annealing process.

5.2 Experimental

Ceramic thin films were deposited on $SiO_2(110)$ substrates by RF magnetron sputtering, using a Zn-enriched target comprised of a homogeneous mixture of 1mol $(Ba_{0.3}Sr_{0.7})(Zn_{1/3}Nb_{2/3})O_3$

and 1 mol ZnO, which were synthesized by a conventional solid-state sintering technique. The monocrystal SiO_2(110) substrates were placed on the substrate holder, which can rotate around a central axis to improve the homogeneity of the thin films. The thin films were deposited using an Ar-O_2 gas mixture in a JGP450 RF magnetron sputtering systerm with the process parameters: 200 W of sputtering power, 0.25 Pa of sputtering pressure, and 610 °C of the substrate temperature. The Ar gas flow rate was fixed at 16 ml/min and the oxygen flow rate was fixed at 3.2 ml/min, i.e., the O_2/Ar flow ratio of 0.2:1 was used as working atmosphere. The distance between the substrates and the targets was 11cm, the sputtering time was 180 min, and the base pressure of the chamber was 1.0×10^{-3} Pa. As-deposited films were annealed in flowing oxygen (99.999%) at 1150 °C for 30 min in a tube furnace.

5.3 Results and discussion

Figure 19 is the X-ray diffraction patterns of the thin films, exhibiting the presence of the well-crystallized thin films. No preferential orientation for the thin film is observed.The thin films contain a mixture of $Ba_{0.5}Sr_{0.5}Nb_2O_6$ (as compared with the JCPDS card of No.39-0265, International Center for Diffraction Data, 2002), $Ba_{0.67}Sr_{0.33}Nb_2O_6$ (No.73-0126), $Sr_{0.744}$Ba0.247Nb_2O_6 (No.70-3747), and $SrNb_2O_6$ (No.72-2088), which can be written as $Ba_xSr_{1-x}Nb_2O_6$. And ZnO is also observed, as compared with the characteristic peak of ZnO. As we all know, the various sputtering yields of Ba, Sr, Nb, Zn, and O elements are a knotty problem in the deposition of $(Ba_{0.3}Sr_{0.7})(Zn_{1/3}Nb_{2/3})O_3$ – based thin films. The discrepancy between thin film and target probably results from the volatilization of ZnO during the process of sputtering and annealing, because Zn has a significant larger vapor pressure than the other metal elements (Ba, Sr, Nb) (Tang et al., 2009). Therefore, ZnO may either not stick to or be re-evaporated from the growing surface (Tang et al., 2009), worsening the composition deviation with the target.

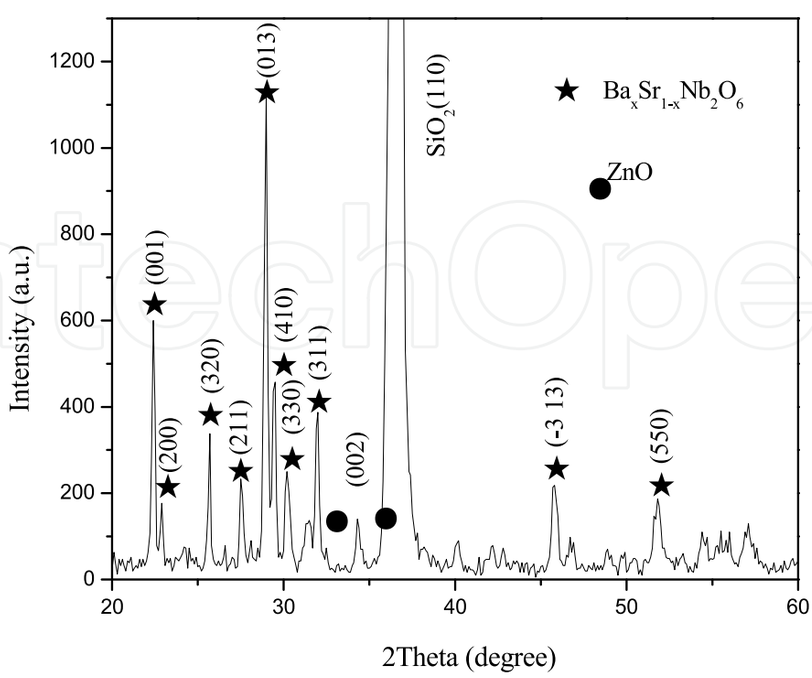

Fig. 19. XRD spectrum of the thin film.

According to the Scherrer`s formula (Ji et al., 2011), the grain size in the (013) plane can be estimated by the following expression:

$$L_{(013)} = \frac{\kappa\lambda}{\beta_0 \cos\theta},$$

where κ is a constant with a value of about 0.89 for the Cu target, λ is the X-ray wavelength with a value of about 1.54718 Å, β_0 is the FWHM of the (013) peak, and θ is the diffraction angle. In the Scherrer`s formula, β_0 = 0.003 rad and θ =29.065°; therefore, the grain size in the (013) plane of the thin film is about 52.76 nm.

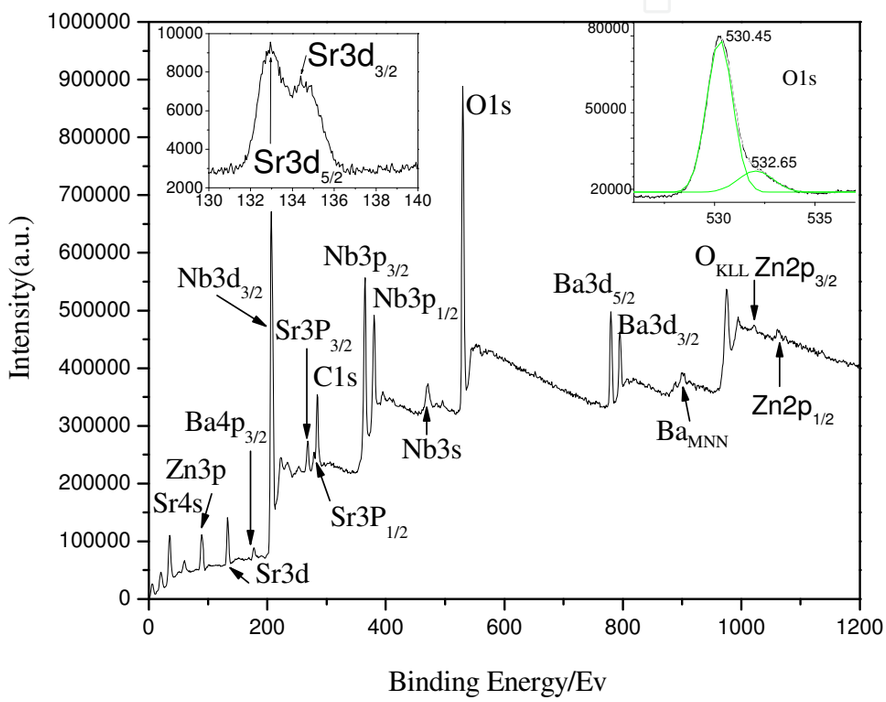

Fig. 20. XPS spectrum of the thin film.

Figure 20 shows the XPS spectrum of the thin film in the binding energy range from 0 eV to 1200 eV, and the binding energies at various peaks were calibrated using the C1s (284.6 eV) as a standard sample. The inset images in Figure 20 shows the XPS spectrum of O1s peak. All the XPS spectra of Ba3d, Nb3d, Sr3d, Sr3p, and Zn2p of the thin films consist of two peaks corresponding to their angular momentum of electron. Only one spin-orbit doublet is observed for the individual element, i.e., $Ba3d_{5/2}$ and $Ba3d_{3/2}$ peaks at 780.67 and 795.95 eV, $Nb3d_{5/2}$ and $Nb3d_{3/2}$ peaks at 206.57 and 209.47 eV, $Sr3d_{5/2}$ and $Sr3d_{3/2}$ peaks at 133.07 and 135.02 eV, $Sr3p_{3/2}$ and $Sr3p_{1/2}$ peaks at 267.84 and 278.37 eV, $Zn2p_{3/2}$ and $Zn2p_{1/2}$ peaks at 1023.27 and 1046.51 eV, indicating that only one chemical state exists in the thin films for each element of Ba, Nb, Sr, Zn, i.e., chemical state of Ba^{2+}, Sr^{2+}, Nb^{5+}, and Zn^{2+}. A doublet structure is observed in the XPS spectrum of O1s peak. Its component peak in the spectrum is fitted to a Gaussian-type distribution with the lower binding energy of 530.45 eV and the higher binding energy of 532.65 eV, as shown in the inset spectrum, corresponding to the

lattice oxygen and the adsorbed oxygen, respectively. In general, the peak of adsorptional oxygen is much weaker than that of lattice oxygen, which would be favorable for the dielectric property of the thin films, because the oxygen vacancies result in the dielectric loss. The quantitative analysis using Ba3d, Sr3d, Zn2p, Nb3d, and O1s peaks reveals that the Ba:Sr:Zn:Nb:O atomic ratio is 3.01: 5.33: 0.96: 27.90: 62.80.

Figure 21. shows the SEM image of the thin film, which shows that fine spherical particles are distributed on the sample's surface. The surface morphology of the thin film is of dense structure with less small holes. It is evident that the grains are of uniform grain size, and are distributed homogenously on the surface of the thin film.

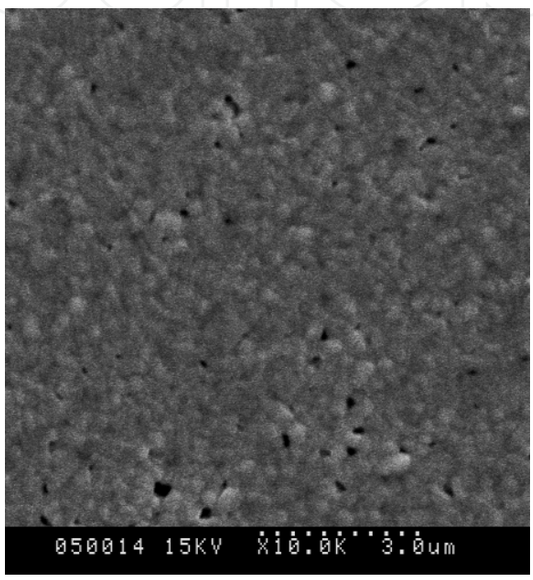

Fig. 21. SEM image of the thin film.

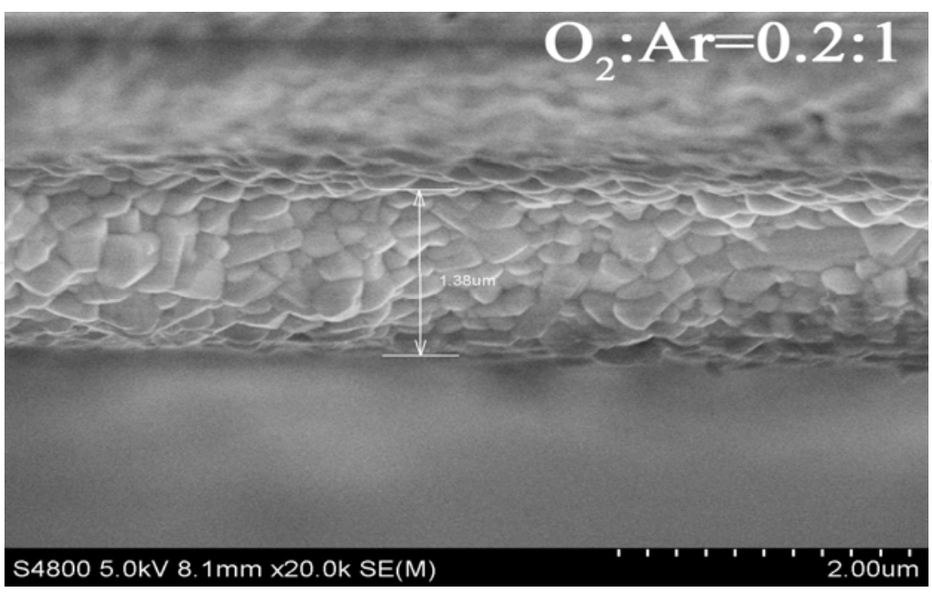

Fig. 22. Cross-sectional SEM images of the thin film.

Figure 22. shows the thickness of the thin film is about 1.38 μm with dense structure and homogeneous grains and well-defined grain boundaries, which are consistent with the results shown in Figure 21.

Figure 23. shows the AFM images of the sample, with a scan area of 10 × 10 μm. As seen in Figure 23(a), the sample is regular in surface with fine and uniform grains, and a few spherical particles are observed growing along the c axis. The root-mean-square surface roughness (RMS, calculated from the AFM data using the PSI ProScan Image Processing software package version 1.0, Park Scientific Instruments, Sunnyvale, CA) of the thin films is about 27.4 nm. Figure 23(b) shows the formation of the ceramic thin film with high-quality crystalline.

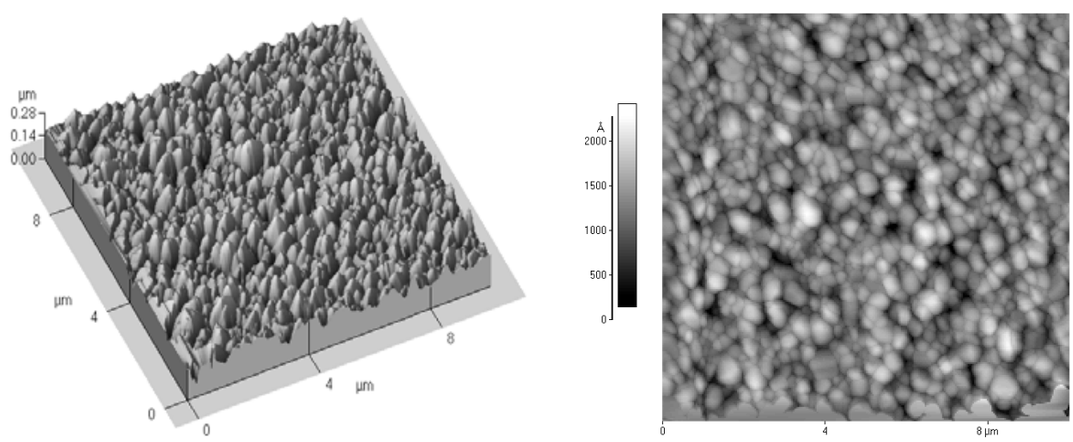

(a) (b)

Fig. 23. AFM images of the thin film. (a) longitudinal cross-section; (b) horizontal cross-section.

The TEM image and the selected area electron diffraction (SAED) spectrum are shown in Figure 24. The spherical particles with the well-defined boundaries are observed in Figure 24(a). The spherical shape of the grains is consistent with the results acquired by the SEM and AFM. The SAED spectrum indicats that the thin films are polycrystalline, as shown in Figure 24(b). About the (013) grain size, there is considerable discrepancy between the measured grain size (approximate 1600 nm by TEM) and calculation size (53 nm obtains from the Scherrer`s formula), which may be because the grain size obtained through the Scherrer`s formula is the average size of the orderly arrangement grains, however, the grain size measured by the TEM is the size of the clusters consisting of many small grains, which have not special periodicity (Ji et al., 2011).

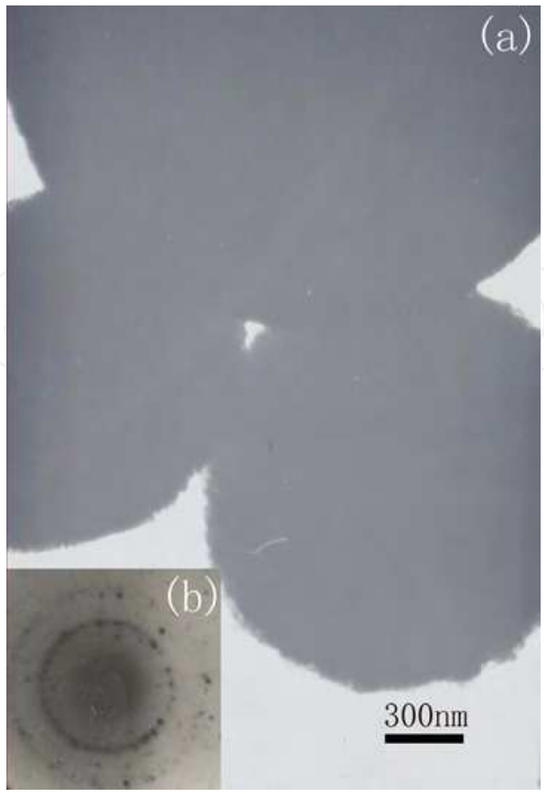

Fig. 24. TEM image and the SAED spectrum of the thin film. (a) TEM; (b) SAED.

5.4 Conclusion

The main phase of the ceramic thin film is $Ba_xSr_{1-x}Nb_2O_6$. The thin film presences a high crystalline quality, with few adsorbed oxygen. The surface morphology indicates that the thin film is of dense structure. The grains are polycrystalline and uniform in size with the spherical shape and well-defined grain boundaries.

6. Acknowledgements

The authors would like to thank the National Natural Science Foundation of China (No.51042001). The authors are also grateful to Professor Chengshan Xue for his help in discussion our results.

7. References

Amanullah, F.M.; Pratap, K.I.; & Hari, V.B. (1998). Compositional Analysis and Depth Profile Studies on Undoped and Doped Tin Oxide Films Prepared by Spray Technique, *Materials Science and Engineering B*, Vol. 52, No.2-3. (April 1998). pp.93-98. ISBN 0921-5107

Cui, C.W.; Shi, F.; Li, Y.G.; & Wang, S.Y. (2010). Orthogonal Analysis for Perovskite Structure Microwave Dielectric Ceramic Thin Films Fabricated by the RF

Magnetron-Sputtering Method, *Journal of Materials Science: Materials in Electronics*, Vol. 21, No. 4, (April 2010), pp. 349-354, ISBN 0957-4522

HSi, C.S.; Chen, C.Y.; Wu, N.C.; & Wang, M.C. (2003). Dielectric Properties of $Ba(Zr_xTi_{1-x})O_3$ Thin Films Prepared Using Radio Frequency Magnetron Sputtering, *Journal of Applied Physics,* Vol. 94, No. 1, (January 2003), pp. 598-604, ISBN 0021-8979

Huang, H.H., Wang, M.C., Chen, C.Y., Wu, N.C., and Lin, H.J. (2006). Effect of Deposition Parameters on the Growth Rate and Dielectric Properties of the $Ba(Sn_xTi_{1-x})O_3$ Thin Films Prepared by Radio Frequency Magnetron Sputtering, *Journal of the European Ceramics Society*, Vol. 26, No. 15, (June 2006), pp. 3211-3219, ISBN 0955-2219

Ianculescu, A.; Despax, B.; Bley, V.; & Lebey, T. (2007). Structure-Properties Correlations for Barium Titanate Thin Films Obtained by RF-Sputtering, *Journal of the European Ceramics Society*, Vol. 27, No. 2-3, (June 2007), pp. 1129-1135, ISBN 0955-2219

Ji, F.F.; Shi, F. (2011). Fabrication and Charicaterization of Ceramic Thin Films by RF Magnetron Sputtering Using Zn - Enriched $(Ba_{0.3}Sr_{0.7})(Zn_{1/3}Nb_{2/3})O_3$ as Target, *Journal of Alloys and Compounds*, Vol.509, No. 5, (Febrary 2011), ppL95-L98, ISBN 0925-8388

Klung, P.; Alexander, L.E. *X-ray diffraction procedures*, John Wiley & Sons, New York,1974.

Liu, L.Y.; Zhu M.K.; Hou, Y.D.; Shao, M.M., & Yan, H. (2005), Effect of Sputtering Pressure on Microstructure of Ferroelectric $Ba_{2-x}TiSi_{2+y}O_8$ Thin Films, *Journal of Wuhan University of Technology,* Vol. 27, No.7, (July 2005). pp.1-3. ISBN 1671-6477

Ma, J.; Feng, J.; Yang, C.S.; & Ding, G.F. (2006). Key Problems in the Preparation of $(Ba,Sr)TiO_3$ Thin Films by RF Magnetron Reactive Sputter Deposition, *Piezoelectrics & Acoustooptics*, Vol. 28, No. 2, (March 2006), pp. 5-8, ISBN 1004-2474

Schroeder, J. B.; Klimasewski, R.G. (1968). Scatter from X-ray Reflecting Surfaces, *Applied Optics,* Vol. 7, No. 10, (October 1968). pp. 1921-1927. ISBN 1559-128X

Shi, F.; Cui, C.W. (2010). Microstructure of Microwave Dielectric Thin Films by RF Magnetron Sputtering, *Applied Surface Science*, Vol. 256, No. 8, (February 2010), pp. 2626-2629, ISBN 0169-4332

Tang, W.Z. (2003), *Theory, Technology and Application for the Fabrication of Thin Film Materials*, Metallurgy Industry Press, Beijing, 2003.

Tang, Z.Z.; Liu, S.J.; Singh, R.K.; Bandyopadhyay, S.; Sus, I.; Kotani, T.; Schilfgaarde, M.; & Newman, N. (2009). Growth and characterization of epitaxial $Ba(Zn_{1/3}Ta_{2/3})O_3$ (1 0 0) thin films, *Acta Materialia*. Vol. 57, No.2, (January 2009). pp.432-440. ISBN 1359-6454

Varma, M.R.; Biju, S.; & Sebastian, M.T. (2006). Preparation of Phase Pure $Ba(Zn_{1/3}Ta_{2/3})O_3$ Nanopowders for Microwave Dielectric Resonator Applications, *Journal of the European Ceramics Society*, Vol. 26, No. 15, pp. 1903 -1907, ISBN 0955-2219

Wang, B.; Wang, M.; Zhang, D.X.; Huang, A.P.; Song, X.M.; Zou, Y.J.; & Yan, H. (2002). Dependence of e-BN Film Structure on Working Pressure and Growth Time, *Functinal Materials*, Vol.33, No. 1, (January 2002). pp. 82-83. ISBN 1001-9731

Wang, C.F. *Solid State Physics Tutorial*, Shandong University Press, Shan Dong, 2004.

Wang, M.C.; HSi, C.S.; & Wu,N.C. (2004). Characterization and Leakage Current Density of Radio Frequency Magnetron Sputtered Nanocrstalline $SrTiO_3$ Thin Films, *Journal of Crystal Growth,* Vol. 264, No. 1-3, (March 2004), pp. 271-277, ISBN 0022-0248

Yang, H.N.; Tweet, D. J.; Ma, Y.J.; & Tue, N.Y. (1998). Deposition of Highly Crosslinked Fluorinated Amorphous Carbon Film and Structural Evolution During Thermal

Annealing, *Applied Physics Letter*, Vol. 73, No.11, (September 1998). pp.1514-1517. ISBN 1882-0778

Yu, L.H.; Fu, X.H. (2006). The Influences of Annealed Temperatures on The Properties and Microstructure of $Ba_{0.5}Sr_{0.5}TiO_3$ Thin Film, *Advanced Ceramics*, Vol. 27, No. 3, (March 2006), pp. 16-19. ISBN 1005-1198

Zannetti, R.; Celotti, G.; Fichera A.; & Francesconi, R. (1969). The Structural Effects of Annealing Time and Temperature on the Paracrystal-Crystal Transition in Isotactic Polypropylene, Die Makromolekulare Chemie, Vol. 128, No.1, (October 1969). pp.137-142. ISBN 0003-3146

Zheng, J.P.; Kwok, H.S. (1993). Preparation of indium tin oxide films at room temperature by pulsed laser deposition, *Thin Solid films*, Vol. 232, No. 1, (September 1993). pp.99-104. ISBN 0040-6090

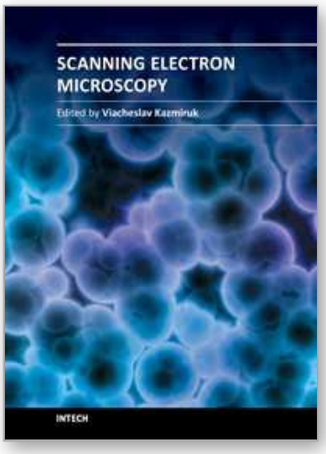

Scanning Electron Microscopy

Edited by Dr. Viacheslav Kazmiruk

ISBN 978-953-51-0092-8
Hard cover, 830 pages
Publisher InTech
Published online 09, March, 2012
Published in print edition March, 2012

Today, an individual would be hard-pressed to find any science field that does not employ methods and instruments based on the use of fine focused electron and ion beams. Well instrumented and supplemented with advanced methods and techniques, SEMs provide possibilities not only of surface imaging but quantitative measurement of object topologies, local electrophysical characteristics of semiconductor structures and performing elemental analysis. Moreover, a fine focused e-beam is widely used for the creation of micro and nanostructures. The book's approach covers both theoretical and practical issues related to scanning electron microscopy. The book has 41 chapters, divided into six sections: Instrumentation, Methodology, Biology, Medicine, Material Science, Nanostructured Materials for Electronic Industry, Thin Films, Membranes, Ceramic, Geoscience, and Mineralogy. Each chapter, written by different authors, is a complete work which presupposes that readers have some background knowledge on the subject.

How to reference

In order to correctly reference this scholarly work, feel free to copy and paste the following:

Feng Shi (2012). Preparation and Characterization of Dielectric Thin Films by RF Magnetron-Sputtering with (Ba0.3Sr0.7)(Zn1/3Nb2/3)O3 Ceramic Target, Scanning Electron Microscopy, Dr. Viacheslav Kazmiruk (Ed.), ISBN: 978-953-51-0092-8, InTech, Available from: http://www.intechopen.com/books/scanning-electron-microscopy/preparation-and-characterization-of-dielectric-thin-films-by-rf-magnetron-sputtering-with-ba0-3sr0-7

INTECH
open science | open minds

InTech Europe
University Campus STeP Ri
Slavka Krautzeka 83/A
51000 Rijeka, Croatia
Phone: +385 (51) 770 447
Fax: +385 (51) 686 166
www.intechopen.com

InTech China
Unit 405, Office Block, Hotel Equatorial Shanghai
No.65, Yan An Road (West), Shanghai, 200040, China
中国上海市延安西路65号上海国际贵都大饭店办公楼405单元
Phone: +86-21-62489820
Fax: +86-21-62489821